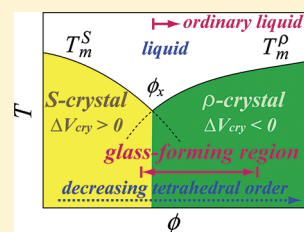


# Relationship between the Phase Diagram, the Glass-Forming Ability, and the Fragility of a Water/Salt Mixture

Mika Kobayashi and Hajime Tanaka\*

Institute of Industrial Science, University of Tokyo, 4-6-1 Komaba, Meguro-ku, Tokyo 153-8505, Japan

**ABSTRACT:** Water is known to be an exceptionally poor glass former, which is a significant drawback in the low-temperature storage of food and biomatter. This is one of the characteristic features of water, but its link to the thermodynamic and kinetic anomalies of water remains elusive. Recently, we showed that the glass-forming ability and the fragility of a water/salt mixture are closely related to its equilibrium phase diagram [Kobayashi, M.; Tanaka, H. *Phys. Rev. Lett.* **2011**, *106*, 125703]. Here we propose that frustration between local and global orderings controls both the glass-forming ability and fragility on the basis of experimental evidence. Relying on the same role of salt and pressure, which commonly breaks tetrahedral order, we apply this idea to pure water under pressure. This scenario not only explains unusual behavior of water-type liquids such as water, Si, and Ge but also provides a general explanation on the link between the equilibrium phase diagram, the glass-forming ability, and the fragility of various materials including oxides, chalcogenides, and metallic glasses.



## I. INTRODUCTION

Water, which is one of the most important substances on the earth, is known to exhibit a number of anomalous behaviors, compared to many other liquids.<sup>1–6</sup> They include the density maximum at 4 °C, the volume increase upon freezing into ice crystal, the anomalous increase in the specific heat at constant pressure and the isothermal compressibility upon cooling, and the decrease of the viscosity with an increase in pressure (up to  $P_x \sim 2$  kbar). Furthermore, water is known as an extremely poor glass former. This problem of glass-forming ability is relevant not only to liquid science but also to biology and food science. Since a sudden volume increase of water upon crystallization leads to serious damage of a biological cell, vitrification of water which does not accompany a discontinuous volume change upon solidification is highly desirable for low-temperature storage of biological cells and foods and is key to cryoprotection for cryopreservation.<sup>7</sup> Despite its practical importance, the physical origin of water's poor glass-forming ability has remained elusive. For example, tremendous efforts have been made to obtain a bulk glassy state of water; however, there is now a consensus that it is impossible to make an amorphous water in bulk with an ordinary cooling procedure. Supercooled bulk water easily crystallizes into ice below its homogeneous nucleation temperature  $T_H$ . Since there is no experimental access to bulk liquid water below  $T_H$ , the temperature region below  $T_H$  is called "no man's land".<sup>3</sup> Recently, computer simulation has started to provide key information to a process of crystal nucleation in bulk water.<sup>8–11</sup>

Although it is difficult or almost impossible to reach a glassy state of bulk water by an ordinary temperature quench, there are still a few other routes (see below) to the formation of bulk amorphous ices<sup>2–4,12</sup> but with an ongoing debate even on the location of the glass-transition temperature  $T_g$ .<sup>13–15</sup> Water can be vitrified by depositing water vapor on a cold substrate (amorphous solid water; ASW) or a rapid cooling at  $10^6$  K/s of emulsified water (hyperquenched glassy water; HWG).

Furthermore, it is known that there exist more than two distinct forms of amorphous ices. Low density (LDA) and high density amorphous ice (HDA) are well-known examples.<sup>3</sup> HDA is obtained by applying a high pressure to ice  $I_h$  at a low temperature. LDA can also be obtained by releasing pressure applied to HDA at a low temperature. LDA produced by heating HDA seems to be identical to ASW and HWG on noting their common amorphous character and density.<sup>3</sup> However, there are several studies which have shown that the local structure of LDA closely resembles that of ice  $I_h$  and  $I_c$ ,<sup>16</sup> whereas the structure of HDA agrees well with that of liquid water. Furthermore, numerous studies of other properties indicate differences between ASW and LDA and/or a link between the local structure of ice  $I_h$  and LDA (see, e.g., refs 17 and 18). This indicates that ASW can be different from LDA. Although this is an interesting issue, it is out of the scope of this paper, and thus we here focus only on the thermodynamic quenching route for vitrification and the resulting amorphous states. Here it is worth noting that the polymorphism of water is suggestive of the existence of more than two liquid states,<sup>3</sup> which still needs to be carefully confirmed.

For pure water, it is known that the anomalous behaviors of water mentioned above and the glass-forming ability are strongly influenced by pressure  $P$ .<sup>4,19</sup> Interestingly, it was shown that the addition of salt has the same effect as the increase of pressure: both lead to the weakening of the anomalies. Furthermore,  $T_H$  decreases with an increase of the salt concentration in a low salt concentration range for a water/salt mixture or with an increase of pressure up to 2 kbar for pure water.<sup>20</sup> For example, a glassy state is more easily obtained for electrolyte solutions.<sup>21–25</sup>

**Special Issue:** H. Eugene Stanley Festschrift

**Received:** April 26, 2011

**Revised:** August 11, 2011

**Published:** September 15, 2011

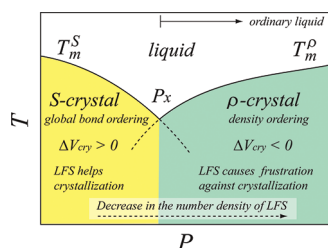


**Figure 1.** Schematic  $P$ – $T$  phase diagram of water-type liquids. The characteristic V-shaped phase diagram basically consists of the two melting curves of different crystal structures, S-crystal and  $\rho$ -crystal (see text). S-crystal is a consequence of global tetrahedral bond ordering. Locally favored tetrahedral structures (LFSs) help crystallization to S-crystal, and thus the glass-forming ability may be low in the S-crystal region. Applying pressure reduces a tendency toward local tetrahedral ordering, which costs a more specific volume. Thus,  $\rho$ -crystal, which is governed by density ordering, is more favored at higher pressure. Since LFS is not consistent with the structure of  $\rho$ -crystal, LFS causes frustration against crystallization into  $\rho$ -crystal and helps vitrification. However, a further increase in  $P$  leads to a decrease of LFSs, which leads to the decrease in the glass-forming ability. The axis  $P$  can be replaced by the salt concentration  $\phi$  for water/salt mixtures since applying pressure and adding salt have the same effect:<sup>26</sup> destroying LFS (see Figure 2).

The critical cooling rate required for vitrification of emulsified water is decreased by about 3 orders of magnitude around 0.2 GPa compared to at ambient pressure.<sup>19</sup> These suggest the similarity between applying pressure and adding salt to water. Indeed, Leberman and Soper compared the effect of salt and pressure, using the intermolecular H–H pair correlation function of water, and found that both effects on water structure are equivalent to each other.<sup>26</sup> Furthermore, Raman scattering studies showed that addition of LiCl to water reduces the local open tetrahedral structure consisting of five water molecules,<sup>27</sup> which we call “locally favored structure (LFS)”. These facts indicate that both salt and pressure act as a breaker of local tetrahedral order (LFS).<sup>28</sup> This suggests that local tetrahedral ordering is a key to the water anomalies and the glass-forming ability.

This equivalence of pressure and salt effects on water structures may be valid as far as we focus on the average properties of water. Their roles as breakers of local tetrahedral order are basically the same. However, there is a crucial difference between pressure and salt effects: The pressure is a homogeneous field, and its increase decreases a bulkier structure such as open tetrahedral structures; whereas ions locally change water structures, and the effects are of local and heterogeneous nature. In relation to this, it may be worth mentioning specific effects of salt ions, which are known as the Hofmeister series. The Hofmeister effects are related to structuring and destructuring effects of ions on the hydrogen bond network of water, which may further be linked to the strength of hydrophobic interactions (see, e.g., ref 29). The specific feature of salt and the local nature of its effect<sup>30</sup> are interesting subjects for future research, but here we concentrate on the global effects of salt.

Some time ago, we proposed that there is an intrinsic link of the thermodynamic phase diagram to the water-type anomalies, the glass-forming ability, and the fragility.<sup>31,32</sup> On the basis of this physical picture, we recently studied experimentally the origin of poor glass-forming ability of water, the fragility of water, and their link to the peculiar V-shaped  $P$ – $T$  phase diagram of water (see Figure 1), by using water/LiCl mixtures as a model system.<sup>33</sup> Here the fragility is a measure of how steeply the viscosity

increases toward  $T_g$ .<sup>2</sup> Liquids with a super-Arrhenius temperature dependence of viscosity  $\eta$  are called fragile liquids, whereas those with an Arrhenius one are called strong liquids. A schematic phase diagram of water-type liquids is shown in Figure 1. Instead of applying pressure, we added salt to control the degree of local tetrahedral ordering since the addition of salt has the same effects as the application of pressure.<sup>32</sup> Thus, we used a mixture of water and LiCl as a model system, following the pioneering works of Angell and his co-workers (see, e.g., refs 21–24), and generalized the salt effect in a water/salt mixture to the pressure effect in pure water. This mixture was also used to investigate the polyamorphism of water.<sup>34,35</sup>

In this paper, we show detailed experimental evidence for an intimate link of the shape of the “equilibrium” phase diagram to the “nonequilibrium” glass transition behavior such as the liquid fragility and the glass-forming ability in water/LiCl mixtures, a part of which was reported in our previous letter.<sup>33</sup> We also discuss the difference of  $T_g$  determination using a cooling and heating differential scanning calorimetry (DSC) scan and propose a method suitable for the fragility determination from the scanning rate dependence of  $T_g$  in DSC. The salt concentration dependence of the transport coefficient is estimated carefully. From this, we demonstrate in an unambiguous manner that a thermodynamic factor coming from energetic frustration plays a crucial role in the glass-forming ability in addition to the kinetic factor. We also explain these experimental findings in detail on the basis of our two-order-parameter model of liquid.<sup>36–39</sup> The organization of this paper is as follows. We describe the experimental details in Section II and the results in Section III. In Section IV we discuss our results in light of our two-order-parameter model of liquid. In Section V, we summarize our work.

## II. EXPERIMENTAL METHODS

We chose a LiCl/water mixture to study effects of modifying water structure by adding salt on the glass-forming ability of water because of the following reason. LiCl can be dissolved in water up to exceptionally high salt concentrations, and at these high concentrations it readily forms a glass upon cooling. In many other aqueous solutions of mineral salts, on the other hand, the salt drops out of a solution as the pure crystal or hydrate, leaving only crystalline ices mixed with water. A LiCl/salt mixture ( $\text{LiCl} \cdot \text{RH}_2\text{O}$ ) is made by mixing LiCl crystals (99.8%, Wako Chemical) with distilled water in a concentration range of  $R = 2.4$ –39. Here  $R$  is the number of water molecules per LiCl molecule: smaller  $R$  corresponds to a higher concentration of LiCl. This range of  $R = 2.4$ –39 corresponds to the molar concentration of LiCl,  $\phi$ , of 29.4–2.5 mol % and the mass concentration of LiCl of 49.5–5.7 wt %.

Differential scanning calorimetry (DSC) measurements were performed by a DSC instrument (Mettler Toledo, DSC822e), which is capable of both conventional (dc) and temperature-modulated (ac) measurements (TMDSC). TMDSC was carried out at the heating rate of 1 K/min, the temperature modulation amplitude of 0.16 K, and the modulation frequency of 60 s. The reversible heat flow was calculated as a ratio of the amplitude of the heat flow modulation to that of modulation in the heating rate. The phase lag was not considered. Viscosity measurements were performed by using a rheometer (Reologica, DAR-100) with the cone plate geometry of diameter 25 mm and angle 4°. The sample temperature was controlled within an accuracy of 0.1 K in the rheometer.

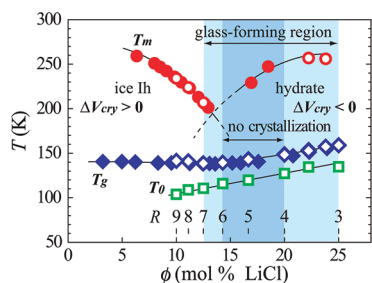


**Figure 2.** Phase diagram of water/LiCl mixtures ( $\text{LiCl} \cdot \text{RH}_2\text{O}$ ) determined by viscosity and DSC measurements. Red circles, melting point  $T_m$ ; blue diamonds, glass-transition temperature  $T_g$ ; green squares,  $T_0$ . Closed symbols are taken from the literature.<sup>25</sup> The similar, but slightly different behavior of  $T_0$ , was reported in the literature.<sup>23</sup> The glass-forming region is determined at a cooling rate of 0.1–20 K/min. The system easily crystallizes for  $R > 7$  (for low  $\phi$ ). With an increase in  $\phi$ , it starts to form a homogeneous glass. The glass-forming ability becomes maximum around  $R = 6$ –4, where we observed no indication of crystallization. A further increase in  $\phi$  leads to easier crystallization ( $R \leq 3$ ).

The DSC protocols used for estimating the fragility of a liquid are as follows: We cooled a sample at a cooling rate  $Q$  down to a temperature  $T_{\min}$  below  $T_g$  and then immediately heated with the same rate to avoid the effects of aging. We chose a different  $T_{\min}$  for each rate and each sample to have the same temperature distance from  $T_g^{\text{cool}}$ , which is estimated from the cooling curve. Following Moynihan's method,  $m$  has often been estimated from  $T_g^{\text{heat}}$ ,  $T_g$  upon heating. However, we also estimated  $m$  from  $T_g^{\text{cool}}$ . We believe that this method provides a more precise estimate of the fragility for a fragile liquid since it is free from superheating effects (see below).

Raman scattering measurements were carried out by a triple-pass Raman spectrometer (HORIBA Jobin Yvon, T64000). We used it in a single monochromator mode and measured both VV and VH Raman scattering signals. We used a single mode solid state laser (Coherent, Verdi-V2, wavelength 532 nm) for the excitation line, and the laser power was less than 100 mW. We used a back scattering geometry, and the polarization of scattered light was selected using a polarizer, which allows us to perform both VV and VH scattering measurements. We used a  $\lambda/4$  plate just before the monochromator to remove the polarization dependence of the spectral efficiency of the grating. The scattering intensity was collected by a 2D detector, a liquid nitrogen cooled CCD (HORIBA Jobin Yvon, Symphony), which enabled us to cover the spectral window at once.

### III. RESULTS

**Phase Diagram.** First we show the phase diagram of a water/LiCl mixture in Figure 2. There are two melting curves, which merge around  $R = 6.5$  and thus have the minimum there. On crystallization, it is known that in the region of  $R > 6$  ice  $\text{I}_h$  precipitates, and the rest of the sample remains a disordered phase;<sup>40</sup> whereas in the region of  $R < 6$ , hydrate crystals of  $\text{LiCl} \cdot \text{RH}_2\text{O}$  are formed. Glass transition behavior is also seen in DSC curves for  $R > 8$ ; however, we also observed an exothermic peak due to crystallization in the cooling curves, indicating partial crystallization. We could not obtain a uniform glassy state for  $R = 9$  even with our highest cooling rate of 20 K/min. A sample of  $R = 9$  showed a steplike viscosity increase upon cooling, which is presumably due to crystallization below 190 K. We never observed

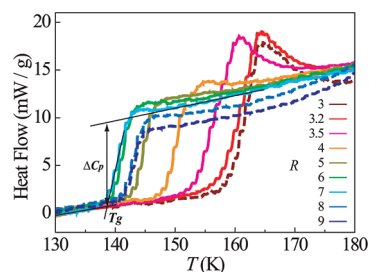


**Figure 3.**  $R$ -dependence of the glass transition behavior. Specific heat of  $\text{LiCl} \cdot \text{RH}_2\text{O}$  measured by temperature-modulated DSC (heating rate = 1 K/min, temperature modulation amplitude = 0.16 K, and the modulation frequency = 60 s). The baseline of the low-temperature side is shifted to 0. The dashed line indicates the existence of partial crystallization upon cooling.

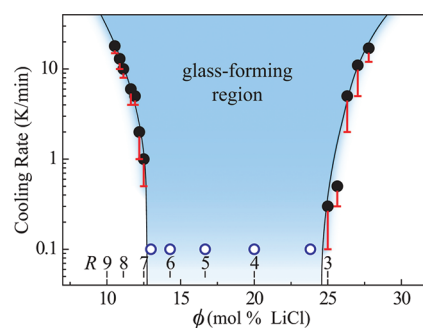


**Figure 4.** Critical cooling rate for vitrification, determined by DSC. Here we define a critical cooling rate as the slowest cooling rate for which we do not observe an exothermic peak due to crystallization in the DSC cooling curve. Crystallization was detected only for cooling rates slower than the error bar. Open circles mean that we never see any crystallization even for our slowest cooling rate of 0.1 K/min, indicating that the critical cooling rate is slower than 0.1 K/min. Solid curves are guides to the eyes. The results clearly show the high glass-forming ability for the intermediate concentration range,  $3 < R < 7$  (see also Figure 2).

crystallization for  $R = 4$ –6. We were able to cool a sample of  $R = 3$  without crystallization in DSC; however, crystallization sometimes takes place on heating above  $T_g$  or even on cooling if we repeated several cooling and heating processes for the same sample. In viscosity measurements under shear, a sample of  $R = 3$  often crystallized on cooling. Thus, we conclude that for  $3 < R < 7$  a uniform glassy state can be formed at a cooling rate of 0.1–20 K/min. This region was determined by DSC, and the details of the measurement method are given below. We also confirmed that the glass-forming ability becomes its maximum for  $R = 4$ –6 (no crystallization), where we never see any indication of crystallization throughout our experiments on both cooling and heating (see Figure 2 and below). The calorimetric glass transition temperature  $T_g$  was measured by the temperature modulated DSC (TMDSC) on heating at 1 K/min, and the heat flow curves are shown in Figure 3 (see Section II for the experimental details). The melting point  $T_m$  was obtained from conventional DSC measurements on heating at 5 K/min for a crystallized sample, where  $T_m$  is a peak temperature of the melting curve. These temperatures are in good agreement with the values reported in the literature<sup>25</sup> (see Figure 2).

**$R$ -Dependence of Critical Cooling Rate.** We show the results of a detailed investigation of the critical cooling rate required for



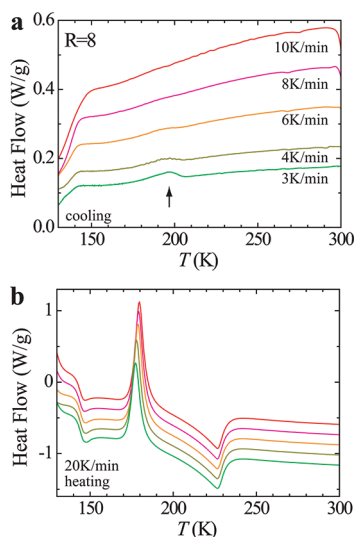


**Figure 5.** DSC curves at several cooling and heating rates for  $\text{LiCl} \cdot 8 \text{H}_2\text{O}$ . (a) DSC curves at a cooling rate of 10, 8, 6, 4, and 3 K/min, from top to bottom. The arrow denotes the position of a slight exothermic heat change due to crystallization. The change in the heat flow below 150 K is due to glass transition. (b) DSC curves at a heating rate of 20 K/min following the cooling at a cooling rate of 10, 8, 6, 4, and 3 K/min, from top to bottom. Plots for 10, 8, 6, and 4 K/min are displaced upward by 0.57, 0.43, 0.28, and 0.14 W/g, respectively, for clarity. The change in the heat flow below 160 K is due to glass transition.

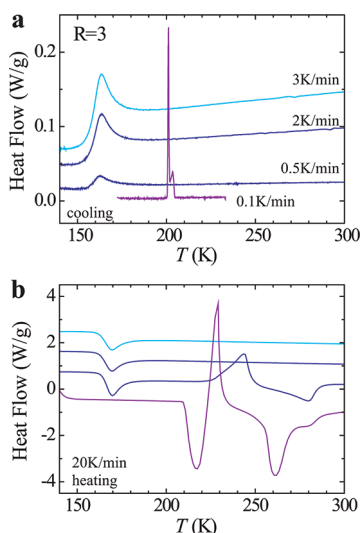


**Figure 6.** DSC curves at several cooling and heating rates for  $\text{LiCl} \cdot 3 \text{H}_2\text{O}$ . (a) DSC curves at a cooling rate of 3, 2, 0.5, and 0.1 K/min, from top to bottom. For the data at 0.1 K/min, we cooled a sample at 10 K/min down to 233 K and applied 0.1 K/min between 233 and 173 K and then cooled at 10 K/min again down to 123 K. The change in the heat flow below 170 K is due to glass transition. (b) DSC curves at a heating rate of 20 K/min following the cooling at 3, 2, 0.5, and 0.1 K/min from top to bottom. Plots for 3, 2, and 0.5 K/min are displaced upward by 2.9, 2.0, and 1.2 W/g, respectively, for clarity. The change in the heat flow below 180 K is due to glass transition. Note that the temperature derivative of the enthalpy  $dH/dT$  is obtained with the opposite sign upon heating in our heat flux DSC.

vitrifying a sample, in Figure 4. We checked whether a sample shows any signature of crystallization or not, as a function of

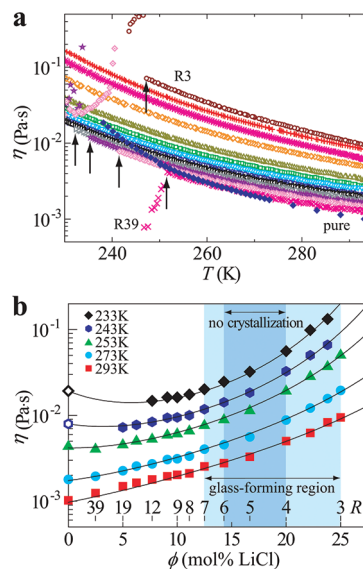


**Figure 7.** Viscosity  $\eta$  of water/LiCl mixtures  $\text{LiCl} \cdot R\text{H}_2\text{O}$  around the supercooled region of pure water. (a) Temperature dependence for  $R = 3, 3.2, 3.5, 4, 5, 6, 7, 8, 9, 10, 12, 15, 19, 39$ , and pure water, from top to bottom. Data were collected during cooling at 1 K/min and a constant shear rate of  $100 \text{ s}^{-1}$ . Arrows denote the discontinuous change in  $\eta$  due to crystallization. The data for pure water are taken from the literature.<sup>103–105</sup> (b)  $\phi$  (or  $R$ )-dependence of  $\eta$ . At low temperatures,  $\eta$  decreases up to about a few mol % and has a minimum around there. Solid curves are theoretical fits of the prediction of the two-order parameter model (see text). The open symbols represent the values of  $\eta$  at  $\phi = 0\%$  estimated by our fittings.

cooling rate. Typical cases at low and high LiCl concentration are shown in Figure 5 and Figure 6, respectively. We cooled a sample at several cooling rates and determined a critical cooling rate as the slowest cooling rate at which we do not observe the exothermic heat signal. We also checked the existence of crystallization by heating each sample at a fixed heating rate of 20 K/min to see if there is an endothermic heat signal due to the melting.

For a low LiCl concentration of  $R = 8$  (Figure 5), there is a small exothermic peak around 200 K at a cooling rate of 3 K/min, and this peak area decreases with an increase in the cooling rate. There is no exothermic heat signal for a rate faster than 10 K/min, and we identified this rate as the critical cooling rate for  $R = 8$ . We can see a signature of glass transition both on cooling and on heating, indicating that the sample does not fully crystallize on cooling. It is consistent with the previous observation that ice  $\text{I}_h$  is precipitated, and the remaining part forms glass (see above). The glassy state of a sample of  $R = 8$  cooled at a rate slower than the critical cooling rate partially contains crystals.

For a high LiCl concentration of  $R = 3$  (see Figure 6), we observed the sharp exothermic peak around 200 K for the data of 0.1 K/min, which indicates crystallization. There is no signature of glass transition on heating of the sample, suggesting that the sample is fully crystallized. Note that there is also a case of partial crystallization for  $R < 3$ . It depends on the LiCl concentration as well as the cooling rate. There were endothermic and exothermic peaks on heating, indicating crystallization, melting, and/or a change in the crystal structure; however, it is difficult to identify the cause of each peak solely from these data. Such complicated behavior is typical for higher LiCl concentrations and absent of low concentrations. This suggests the presence of a few phase

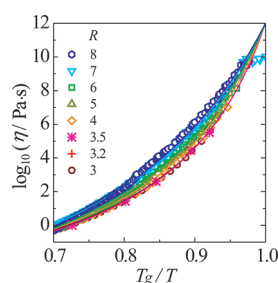


**Figure 8.** Angell plot of the viscosity  $\eta$  for water/LiCl mixtures ( $\text{LiCl} \cdot \text{RH}_2\text{O}$ ) for several LiCl concentrations. We can see a clear  $R$ -dependence of the fragility: The liquid becomes more fragile with a decrease in  $R$  (i.e., an increase in  $\phi$ ). The solid curves are VFT fits to the data. The temperature is scaled by  $T_g$ , which is determined as a temperature where the extrapolated viscosity of the Vogel–Fulcher–Tammann (VFT) relation becomes  $\eta = 10^{12} \text{ Pa} \cdot \text{s}$ . Data were collected during cooling at 1 K/min (5 K/min for  $R = 3$ ). The numbers represent the values of  $R$ .

transition processes at high  $\phi$  and the presence of just one crystal at low  $\phi$ . For cooling rates faster than 0.3 K/min, there is no change in the heat flow above 170 K. That is, the sample can be cooled without crystallization. There is a pair of exothermic and endothermic peaks on heating at 0.5 K/min (see Figure 6), indicating that the system is crystallized and then melts on heating. For a rate faster than 2 K/min, there was no crystallization on heating. The glass transition on cooling exhibits a peak at its high-temperature side. We note that this peak is not due to crystallization because there is no signal from the melting of a crystal upon heating. Furthermore, the peak is observed as the reversible heat flow of the temperature modulated DSC. The origin of this peak thus remains elusive at this moment.

These results clearly show the regions where a system is crystallized or vitrified as a function of the salt concentration and the cooling rate. We identify a stable glass-forming region as  $3 < R < 7$  (see Figure 4). Open symbols denote the LiCl concentration at which there was no signature of crystallization even at our slowest cooling rate of 0.1 K/min. It is worth mentioning that  $R = 7$  almost corresponds to  $R_{\text{min}}$ , where the melting point  $T_m$  has the minimum (see Figure 2). Thus, the glass-forming ability becomes maximum when the equilibrium crystal to be formed changes from ice  $I_h$  to hydrate crystals.

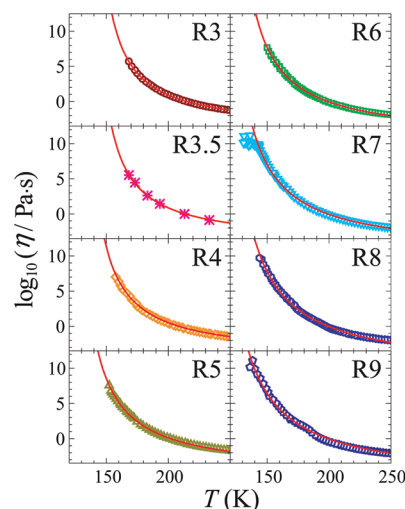
**Results of Viscosity Measurements and the Estimation of the Fragility.** Next, we show the temperature ( $T$ ) and LiCl concentration ( $\phi$ ) dependence of the shear viscosity  $\eta$  in Figure 7 and Figure 8. The viscosities of water/LiCl mixtures at rather high temperatures were reported and discussed by Angell et al. in their pioneering work.<sup>23,24</sup> Here we accessed a temperature to near  $T_g$  and thus covered an almost entire supercooled region. Data were collected during cooling at 1 K/min.

Figure 7(b) is the  $\phi$ -dependence of  $\eta$  for a temperature range from room temperature to the supercooled region of pure water. The viscosity  $\eta$  monotonically increases with an increase in  $\phi$  above 273 K; however, the  $\phi$ -dependence becomes nonmonotonic at low temperatures. At  $T = 253 \text{ K}$ , for example, the viscosity  $\eta$  decreases with an increase in  $\phi$  up to 2.5 mol % ( $R = 39$ ), reaches a minimum around there, and then increases with a further increase in  $\phi$ . At 243 K,  $\eta$  for pure water is significantly larger than that for  $\phi = 5 \text{ mol } \%$  ( $R = 19$ ), and a minimum must exist between 0 and 5 mol %. This behavior is strikingly similar to the pressure dependence of  $\eta$  of pure water.<sup>32,41,42</sup> When applying

**Table 1.** Dependence of the Glass Transition Temperature  $T_g$  and the Ideal Glass Transition Temperature  $T_0$  on  $R$  for Water/LiCl Mixtures ( $\text{LiCl} \cdot \text{RH}_2\text{O}$ )<sup>a</sup>

$R$	3	3.5	4	5	6	7	8	9
$T_g \text{ (K)}$	159	153	148	143	139	139	141	141
$T_0 \text{ (K)}$	135	134	127	120	116	111	109	104

<sup>a</sup> We estimated  $T_g$  from the low-temperature edge of the reversing heat flow measured by temperature modulated DSC (TMDSC) at a heating rate of 1 K/min (Figure 3) and  $T_0$  from the VFT fits to the viscosity data in Figure 8.



**Figure 9.** Temperature dependence of the viscosity  $\eta$  for water/LiCl mixtures ( $\text{LiCl} \cdot \text{RH}_2\text{O}$ ) for eight LiCl concentrations. The solid curves are the results of the VFT fits to the data. The data were collected during cooling at 1 K/min (5 K/min for  $R = 3$ ).

pressure to pure water at low temperatures,  $\eta$  first decreases with increasing  $P$  up to around 2 kbar, exhibits a minimum there, and then starts to increase with further increasing  $P$ . Thus, this also supports the equivalence of increasing the salt concentration in a water/salt mixture and applying the pressure to pure water.

Figure 8 is the  $T$ -dependence of  $\eta$  in the form of an Angell plot.<sup>2</sup> The viscosity data in the glass-forming region ( $3 < R < 7$ ) exhibit a clear  $R$ -dependence: the temperature dependence of the viscosity becomes stronger with a decrease in  $R$ . This means that the system monotonically becomes more fragile with an increase in the LiCl concentration,  $\phi$ . We analyzed these data by fitting the Vogel–Fulcher–Tammann (VFT) relation

$$\eta = \eta_0 \cdot \exp(DT_0/(T - T_0)) \quad (1)$$

where  $\eta_0$ ,  $D$ , and  $T_0$  are the fitting parameters.  $D$  is the so-called fragility index, but note that larger  $D$  means less fragile.  $T_0$  is the VFT temperature, where  $\eta$  hypothetically diverges. The  $\phi$ -dependence of  $D$  is shown in Figure 10. The value of  $D$  becomes smaller and  $T_0$  monotonically increases with an increase in  $\phi$  (or a decrease in  $R$ ) (see Table 1 and Figure 2). The viscosity data and the VFT fits for them are shown in Figure 9. The viscosity data higher than  $10^{10} \text{ Pa} \cdot \text{s}$  may contain significant experimental errors since they are beyond the high viscosity limit of our rheometer. Thus we did not include these data in our VFT fittings.

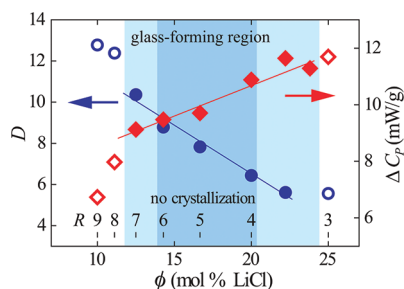


**Figure 10.**  $\phi$  (or  $R$ )-dependence of the fragility index  $D$  (circles) and  $\Delta C_p$  (diamonds). Open symbols are obtained from partially crystallized samples. The fragility index  $D$  is estimated by the VFT fitting to the viscosity in Figure 8. A smaller value of  $D$  means that a liquid is more fragile. The value of  $\Delta C_p$  is estimated from Figure 3 as a magnitude of the step in  $C_p$  across  $T_g$ . A larger value of  $\Delta C_p$  is typically observed in a more fragile liquid. Solid lines are guides to the eyes.

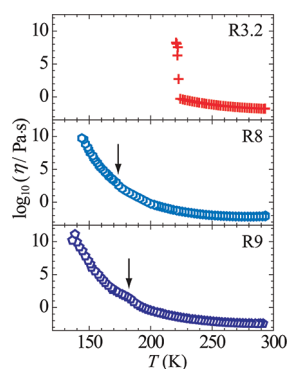


**Figure 11.** Temperature dependence of  $\eta$  of water/LiCl mixtures  $\text{LiCl} \cdot R\text{H}_2\text{O}$  for  $R = 3.2, 8$ , and  $9$ , where each sample shows crystallization on cooling. Nonmonotonic or discontinuous changes in the temperature dependence are due to crystallization. The drastic increase in  $R = 3.2$  suggests that the whole sample crystallizes, whereas the gradual winding (arrow) in  $R = 8$  and  $9$  indicates partial crystallization. Data were collected during cooling at  $1 \text{ K/min}$ .

We observed indications of crystallization at low ( $R \geq 8$ ) and high ( $R \leq 3.5$ ) LiCl concentration in viscosity measurements, as shown in Figure 11. A sample of  $R \geq 8$  showed a steplike change in the temperature dependence of  $\eta$ . For example, we can see slight windings in the data for  $R = 9$  around  $190 \text{ K}$  and for  $R = 8$  around  $170 \text{ K}$ . The winding is presumably due to partial crystallization, and the data at low temperatures indicate there remains fluidity, suggesting that isolated crystals are immersed in the matrix of a supercooled liquid. For crystallization at high LiCl concentrations (for example,  $R = 3.2$  in Figure 11), on the other hand,  $\eta$  increases by several orders of magnitude, indicating that the whole sample becomes solid immediately or crystals are at least percolated. We point out that there is a systematic difference in crystallization behavior between viscosity and DSC measurements: we observed crystallization on cooling under shear in a concentration range  $R = 3\text{--}3.5$ , whereas we did not observe crystallization for the same cooling rate of  $1 \text{ K/min}$  for DSC measurements. This difference implies that there are shear effects on crystallization.

**Results of DSC Measurements of the Glass Transition and the Estimation of the Fragility.** The specific heat  $C_p$  exhibits a steplike change across  $T_g$  (see Figure 3). The magnitude of this

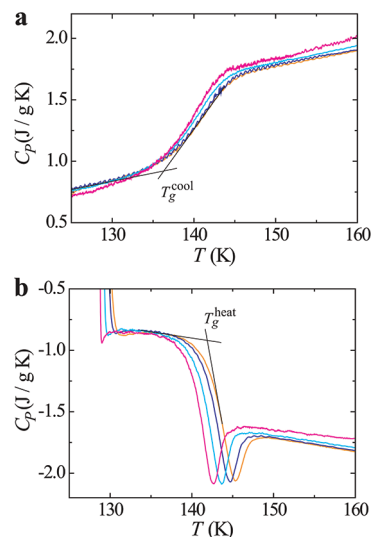


**Figure 12.** DSC curves around the glass transition region, for the fragility determination of  $\text{LiCl} \cdot 5\text{H}_2\text{O}$ . (a) DSC cooling curves. Cooling rate dependence of the glass transition temperature at  $Q_{\text{cool}} = 3, 2, 1$ , and  $0.5 \text{ K/min}$  was estimated to be  $T_g^{\text{cool}} = 136.4, 136.4, 136.0$ , and  $135.5 \text{ K}$ , respectively. (b) DSC heating curves. Samples were heated after cooling to  $T_{\text{min}} = T_g^{\text{cool}} - 7 \text{ K}$  at the same rate:  $Q_{\text{heat}} = Q_{\text{cool}}$ . Heating rate dependence of the glass transition temperature at  $Q_{\text{heat}} = 3, 2, 1$ , and  $0.5 \text{ K/min}$  was estimated to be  $T_g^{\text{heat}} = 141.9, 141.4, 140.5$ , and  $139.7 \text{ K}$ , respectively. Oscillations in the data are due to the system noise.

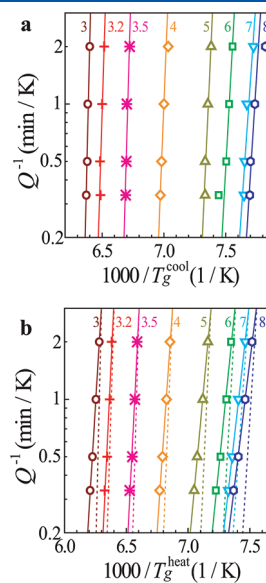


**Figure 13.**  $R$ -dependence of the glass transition behavior. Here the inverse of the rate  $Q$  (the characteristic time scale) is plotted against the inverse of  $T_g$  in a manner coherent to the Arrhenius-like plot. (a) Cooling rate ( $Q$ ) dependence of  $T_g^{\text{L}}$  determined by DSC measurements for  $\text{LiCl} \cdot R\text{H}_2\text{O}$ . (b) Heating rate ( $Q$ ) dependence of  $T_g^{\text{L}}$  for  $\text{LiCl} \cdot R\text{H}_2\text{O}$ . In both (a) and (b), the numbers in the figure are the value of  $R$ , and the straight lines are results of the linear fits. For both cases, the slope becomes steeper with an increase in  $\phi$  (or a decrease in  $R$ ), indicating that the liquid becomes more fragile with  $\phi$ . The dashed lines in (b) have the same slopes as the fitting results in (a) at each concentration. We can clearly see that the cooling rate dependence is weaker than the heating rate dependence.



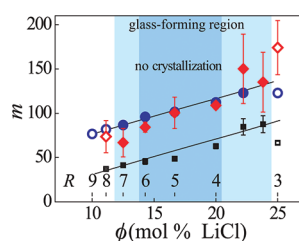


**Figure 14.**  $\phi$  (or  $R$ )-dependence of the fragility parameter  $m$ . Diamonds and squares are estimated from the scanning rate dependence of the glass transition temperature  $T_g$  measured by DSC upon cooling and heating, respectively. Circles are values converted from the fragility index  $D$  in Figure 10, which is determined from the viscosity data. All the data indicate that a system of smaller  $R$  (higher  $\phi$ ) is more fragile (larger  $m$ ). The values of  $m$  evaluated from  $T_g$  upon cooling well agree with those from the viscosity data even on a quantitative level, whereas those from  $T_g$  upon heating are smaller than the other two data. Open symbols denote the data for partially crystallized samples. Solid lines are guides to the eyes.

step,  $\Delta C_p$ , estimated from Figure 3 is plotted in Figure 10. A large  $\Delta C_p$  is characteristic of a fragile liquid.<sup>43</sup> The larger  $\Delta C_p$  for smaller  $R$  is consistent with the results of viscosity measurements that a liquid with smaller  $R$  has a steeper change of viscosity (smaller  $D$ ) and thus is more fragile.

We also estimate the fragility parameter  $m$ , which is defined as a slope of the temperature dependence of the relaxation time  $\tau$  at  $T_g$ .<sup>44,45</sup>

$$m \equiv \left. \frac{d(\log_{10}(\tau))}{d(T_g/T)} \right|_{T=T_g} \quad (2)$$

Note that larger  $m$  means more fragile. To estimate  $m$ , we studied the scanning rate  $Q$  dependence of  $T_g$  in DSC measurements.<sup>46,47</sup> Typical DSC curves obtained by this protocol are shown in Figure 12.

Figure 13(a) and (b) shows the  $Q$ -dependence of  $T_g^L$ , which was estimated from the low-temperature edge of the DSC curve upon cooling and heating, respectively (see Section II for the DSC protocols used). We can see that the  $Q$ -dependence of  $T_g^L$  becomes weaker with a decrease in  $R$ . We estimated the value  $m$  in eq 2 from the slope of the straight line fitted to the data. The results are shown in Figure 14 with the possible errors involved in the fitting: Diamonds are  $m$  estimated from cooling experiments, whereas squares are from heating experiments. The large errors in estimating  $m$  for cooling are because the scanning rate dependence of  $T_g$  on cooling is weaker than that on heating. For comparison, we also show the values of  $m$  estimated from our viscosity measurements, using the following relation between  $m$  and  $D$  (see Figure 14)

$$m = (D/\ln 10) \cdot (T_0/T_g) \cdot (1 - (T_0/T_g))^{-2} \quad (3)$$

Three kinds of estimation show qualitatively the same trend. The  $m$  estimated from  $T_g^{\text{cool}}$  very well agrees with that from viscosity measurements even on a quantitative level. The results clearly indicate the increase of  $m$  with a decrease in  $R$ : a decrease in  $R$  makes a water/salt mixture more fragile.

**Possible Origins of the Difference in the Fragility Determined by Different Methods.** The differences in the fragility determined by different methods have been reported in the literature.<sup>48–50</sup> The value  $m$  obtained from the scanning-rate ( $Q$ )

dependence of  $T_g$  measured by DSC is often smaller (i.e., stronger or less fragile) than that estimated from other dynamical (viscosity or dielectric relaxation) data. This difference is known to be more pronounced for fragile liquids.<sup>48,50</sup> For example, we estimated  $m$  for glycerol (upon heating), which is known as a rather strong glass former, as  $m = 50$  from the scanning-rate dependence of  $T_g^{\text{heat}}$ . This value agrees well with that estimated from dielectric relaxation data.<sup>51</sup>

We argue that the difference arises from superheating effects. The DSC curve reflects the temperature dependence of the structural relaxation time  $\tau$ . The value of  $\tau$  is not constant in the transition region, and thus  $T_g$  does not necessarily correspond to  $\tau$  at that temperature. The time range involved is larger for heating than for cooling since the glass transition on heating marks the temperature above which the system starts to be able to follow the heating rate, while that on cooling marks the temperature below which the system starts to fail in following the cooling rate. Thus,  $m$  estimated for cooling should be more accurate. Nevertheless, these types of measurements have mostly been performed *upon heating*. This effect of superheating should be more pronounced for a more fragile system exhibiting a steeper temperature dependence of  $\tau$ . For a fragile system, the range over which  $\tau$  changes in the transition region should strongly depend on the location of the transition temperature. For a strong liquid, on the other hand, that range should be independent of the transition temperature. Another merit of estimating  $m$  for cooling is that heating experiments also suffer from aging effects,<sup>47,52,53</sup> which are more serious for a more fragile liquid. Here we note, however, that in our protocol we can avoid the effects of aging, as described in Section II.

Furthermore, the difference between the estimation from viscosity and DSC measurements can also arise from the time range used for analysis. Note that DSC measurements can access a time scale of only about a decade very near  $T_g$ , whereas dynamical measurements usually cover a much wider time range (often, more than ten decades): As shown in Figure 8, our viscosity measurements cover nearly 10 decades. Since the structural relaxation time of a fragile liquid increases so steeply near  $T_g$ , there may be a rather large experimental error in the determination of  $m$  by DSC.

**Direct Estimation of the  $\phi$ -Dependence of the Fraction of Locally Favored Tetrahedral Structures by Raman Scattering Measurements.** Here we consider how we can estimate the  $\phi$ -dependence of the fraction of locally favored tetrahedral structures  $S$  (note that  $S$  is “not” entropy) in liquid water and a LiCl/water mixture. Walrafen<sup>54</sup> reported that the  $T$ -dependence of the Raman spectrum in the OH stretching region provides information key to the two-state model of water. He also studied the effects of adding salt to water.<sup>55</sup> Green et al.<sup>56</sup> reported that the low-frequency shoulder of the Raman spectrum in the OH stretching region can be used as a probe of in-phase collective motions specific to tetrahedrally coordinated water structures. Recent numerical simulations supported this view by comparing the distribution of the tetrahedral order parameter  $q$  of a model water (SPC/E) with the shape of Raman scattering spectra.<sup>57</sup> Green et al.<sup>27</sup> also applied their method to a LiCl/water mixture and found that the addition of LiCl to water leads to breakup of tetrahedral structures without significantly alternating the hydrogen bonding energy distribution. So we employed their method to estimate the fraction of locally favored tetrahedral structures as a function of the LiCl concentration  $\phi$ .

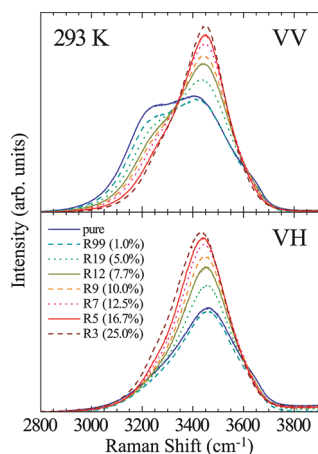


**Figure 15.**  $\phi$ -dependence of VV and VH Raman spectra of water/LiCl mixtures around the frequency region of OH stretching modes at 293 K. The low frequency component around 3200  $\text{cm}^{-1}$  in the VV spectrum which is related to the tetrahedral order of water molecules decreases with an increase in the LiCl concentration.

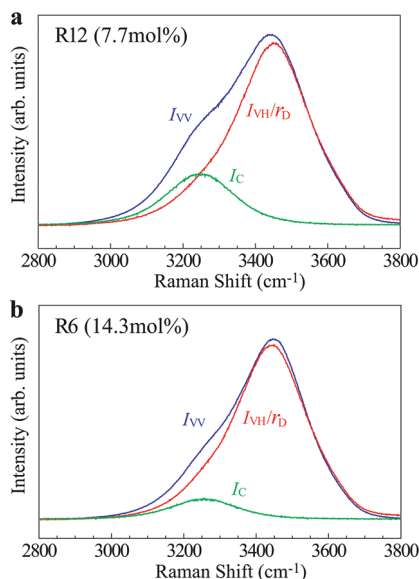


**Figure 16.** Example of the decomposition of the VV Raman spectrum of water/LiCl mixtures in the OH stretching region for (a)  $R = 12$  ( $\phi = 7.7$  mol %) and (b)  $R = 6$  ( $\phi = 14.3$  mol %) at 293 K. In-phase collective spectrum  $I_c$  is extracted from VV and VH Raman spectra. The area of  $I_c$  is proportional to the number density of tetrahedral structures of water molecules.

The change in the VV scattering spectrum in the OH stretching region as a function of  $\phi$  is shown in Figure 15. We can clearly see that the intensity of the low-frequency shoulder decreases with an increase in  $\phi$ , as reported in the literature.<sup>27</sup> Following the procedure of Green et al.,<sup>27,56</sup> we estimated the relative strength of the in-phase collective spectrum defined by

$$C = \int I_c(\omega) d\omega / \int I_{VV}(\omega) d\omega \quad (4)$$

Here  $I_{VV}$  is the VV scattering intensity,  $I_c = I_{VV} - r_D^{-1} I_{VH}$ ;  $I_{VH}$  is the VH scattering intensity; and  $r_D$  is the depolarization ratio (see refs 27 and 56 for the details of the analysis). An example of such

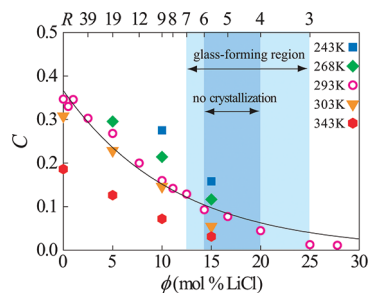


**Figure 17.**  $\phi$ -dependence of the relative strength of the in-phase collective spectrum. Open circles are our data at 293 K, and solid curves are fits to our exponential function (see text). Closed symbols are data from the literature.<sup>27</sup>

a decomposition is shown in Figure 16. The  $C$  estimated in this way is plotted as a function of  $\phi$  in Figure 17, together with the data reported by Green et al.<sup>27</sup> We can see that our results are consistent with those of Green et al.

We used our two-state picture to estimate the tetrahedrality and accordingly decomposed each Raman spectrum into two components, as shown above. Here it may be worth mentioning that there are some arguments on which of the two-state (or mixture) model and the continuum model is more appropriate for the physical description of the structure of liquid water and the Raman spectrum.<sup>58–60</sup> In our two-state model, water molecules are grouped into two types: hydrogen-bonded water molecules forming long-lived tetrahedral structures and the other water molecules (see below). Thus, the tetrahedrality is directly linked to the number density of tetrahedral structures. In the continuum model, on the other hand, all water molecules are hydrogen bonded, and the degree of distortion is distributed continuously. The tetrahedrality is thus given by the degree of tetrahedral order. The relationship between Raman and IR spectra and the tetrahedrality has been studied on the basis of both the two-state (or mixture) and continuum model. However, the tetrahedralities estimated by these two types of models coincide with each other.<sup>61–63</sup>

As will be shown below, we employ a two-state model. We argue that the local tetrahedral symmetry has a strong effect on the stability of structural motifs, and only the tetrahedral structures are considerably longer-lived than the other structures, which we call “normal liquid structures”: formation of a tetrahedral structure stabilizes hydrogen bondings with the help of its symmetry in a “cooperatively” manner. We note that normal liquid structures do not mean structures of water molecules forming no hydrogen bonds but rather those without high tetrahedral symmetry. Thus, we group water structures into those acting as the local symmetry element and those having no particular symmetry. Although the validity of this model should be carefully checked, recent numerical simulation studies seem to support our scenario<sup>64,65</sup> (see also below).

## IV. DISCUSSION

**Brief Review of Our Two-Order-Parameter Model of Liquid.** First, we review our two-order-parameter model of the liquid–glass transition,<sup>36–39</sup> which we use to explain our observations. This model focuses on a general tendency of a liquid to form locally favored structures. Although there can be more than two candidates for such local structures, here we stick to the simplest picture of a liquid, which approximately has only two energy levels: (a) normal-liquid structure (NLS), which is a high



energy state (short-lived), and (b) locally favored structure (LFS), which is a low energy state (long-lived). We define the energy gain and volume change upon the transformation from NLS to LFS as  $\Delta E \equiv E_{\text{NLS}} - E_{\text{LFS}}$  (always positive by definition) and  $\Delta V \equiv V_{\text{LFS}} - V_{\text{NLS}}$  (for water  $\Delta V > 0$ ).

In this model, structural frustration between LFS and the equilibrium crystal structure plays a significant role in vitrification.<sup>36–39,66</sup> LFS is a structure formed to “locally” minimize the potential energy while paying an entropic penalty, and thus its symmetry is not necessarily consistent with the symmetry of the equilibrium crystal which is a result of “global” minimization of the free energy. If LFS is not consistent with the crystal structure, then LFS acts as a source of frustration, or impurity, against crystallization to the equilibrium crystal.<sup>36–39,66–68</sup> This competition between the two types of orderings, local vs global, would help a liquid to bypass crystallization and vitrify upon cooling. Thus, the increase in the degree of frustration is expected to increase the glass-forming ability. This was confirmed by our numerical simulations.<sup>67–70</sup>

In usual liquids, an equilibrium crystal is stabilized mainly by intermolecular attractions (e.g., van der Waals attractions), and thus the density is increased upon crystallization. We refer this type of crystallization to density ( $\rho$ ) ordering and the resulting crystal to  $\rho$  crystal. On the other hand, LFS is usually stabilized by directional bonding (hydrogen bonding or covalent bonding), and we refer this type of ordering to bond ( $S$ ) ordering. In some cases, a system can attain global bond ordering or form a crystal stabilized by directional bonding. We refer to this type of crystal as  $S$ -crystal (see Figure 1). We note that  $S$ -crystal has a specific volume larger than its liquid state for a system of  $\Delta V > 0$ , as in water: for water  $\Delta V_{\text{cry}} > 0$ , where  $\Delta V_{\text{cry}}$  is an amount of the increase in the specific volume upon crystallization from a liquid.

Fragility is determined by the degree of frustration between LFS and crystal structure in our model. Stronger frustration leads to a larger distance between the onset temperature of cooperativity (near the melting point) and the VFT temperature  $T_0$ , where the relaxation time is assumed to diverge.<sup>36–39</sup> This larger distance between the onset and the diverging point means a slower (more Arrhenius-like) increase in  $\eta$ , or the structural relaxation time, upon cooling, indicating that a liquid is stronger. Since stronger frustration leads to a better glass-forming ability in our model, our model predicts a negative correlation between the fragility and the glass-forming ability,<sup>36–39</sup> provided that the other thermodynamic factors are not so different.

We proposed that water anomalies can primarily be explained by a simple two-state model based on this picture,<sup>42,71</sup> although some cooperativity in  $S$  ordering might also play a role.<sup>3,71–73</sup> In the case of water, we argue that water is also made of two states: NLS, where van der Waals attractions lead to a higher local density (density  $\rho$  ordering), and LFS, which has an open tetrahedral structure with a lower density (bond  $S$  ordering). Here we emphasize that NLS is a highly degenerate state with large entropy and energy (large degeneracy  $g_\rho$ ), whereas LFS is a state of low entropy and energy (small degeneracy  $g_S$ ) because of a specific symmetry (or uniqueness) of its structure. This reflects the fact that LFS is fully stabilized by hydrogen bondings, whereas NLS is under competition between hydrogen bonding and van der Waals interactions and thus frustrated. We stress that it is this high entropy nature of NLS that makes NLS more favorable at higher temperature. This simple two-state model well explains the thermodynamic and kinetic anomalies of water.<sup>32,42,71</sup> Here we note that for water both NLS and LFS

are dominated by hydrogen bonding but with less tetrahedrality for the former (see e.g., ref 71). More specifically, LFS of water is linked to a local open tetrahedral structure,<sup>32,42,71</sup> which is made of five water molecules and stabilized by hydrogen bonding.<sup>1–6</sup> Because of the phenomenological nature of our model, we cannot specify the very structure of LFS, and we can only suggest it has a link to open tetrahedral order for water. We may need to consider a structural feature associated with the second shell distance, as pointed out in the literature.<sup>6</sup>

Here we mention some of the numerical simulation works closely related to what is described above. Recently, it was shown that the steep decrease in the entropy upon cooling is due to the development of tetrahedral order.<sup>74</sup> This means that local structural ordering is a key to the anomalies. Furthermore, the link between structure, entropy, and diffusivity has also been clearly demonstrated for model waters.<sup>75</sup> This work also showed that water anomalies occur at much lower pressure than  $P_x$ . In our view, this is related to the pressure dependence of  $S(T, P)$ . The prediction of our model on this  $T$ -dependence of  $S$  was also supported by numerical simulations,<sup>64,65</sup> in which the identification of the inherent structure and the characterization of tetrahedral structural order parameter are nicely combined.

On the basis of this picture, we consider what makes water so special and unusual. As mentioned above, molecular liquids usually interact with van der Waals and hydrogen bonding interactions. Among various molecular liquids, water is a molecular liquid which has the maximum fraction of the contribution of hydrogen bonding in the total interaction energy. Another unique feature is the consistency of the symmetry of LFS to the equilibrium crystal. The crystal structure of water at ambient pressure is well-known hexagonal ice  $I_h$ . Ice  $I_h$  is not a high-density packed  $\rho$ -crystal but a low density  $S$ -crystal, which is mainly stabilized by hydrogen bonding with an open structure (see Figure 1).<sup>32,42,71,76</sup> Thus, the structure of ice  $I_h$  is (almost) consistent with the tetrahedral structure of LFS. This means that for water at ambient pressure crystallization can at least approximately be regarded as global  $S$ -ordering, and thus LFS helps crystallization rather than interferes with it. We propose that this weakness (or absence) of frustration against crystallization into ice  $I_h$  is one of the primary (thermodynamic) reasons why water is such a poor glass former.<sup>32,42,71,76</sup> This scenario seems to be consistent with the microscopic process of crystal nucleation in water.<sup>8</sup> A link between local structural ordering and water anomaly has also been supported by simulation studies (see, e.g., refs 64, 65, 74, 75, and 77–82).

With increasing pressure, however, the crystal structure changes from hexagonal ice  $I_h$  to tetragonal ice  $III$  at a critical pressure  $P_x$  ( $\sim 2$  kbar), where the two melting curves merge and the melting point has a minimum. This leads to the density increase of the crystal from 0.92 to 1.14 across  $P_x$ ,<sup>83</sup> and above  $P_x$  the anomalous volume increase upon crystallization disappears and  $\Delta V_{\text{cry}}$  becomes negative there. We may say that the crystal structure changes from  $S$ -crystal to  $\rho$ -crystal at  $P_x$  (see Figure 1). Water should behave as an ordinary liquid above  $P_x$  according to our scenario. We expect the increase of the glass-forming ability near  $P_x$ , but it should decrease again with a further increase in  $P$ . This is because the number density of LFS,  $S$  (“not” entropy), which is a source of frustration against crystallization into  $\rho$ -crystal, should monotonically decrease with an increase in  $P$  as

$$S \cong g_S/g_\rho \exp[(\Delta E - P\Delta V)/k_B T] \quad (5)$$

where  $k_B$  is Boltzmann's constant (note for water  $\Delta V > 0$ ).<sup>32,42,71,76</sup>

We emphasize that our model is different from the so-called mixture models of water, which regard a liquid as a mixture of only two structural motifs (e.g., LDA and HDA). These models do not take into account the large entropy change associated with the transformation between the two states (in our case, LFS and NLS) since both LDA and HDA are treated as a unique structure with a degeneracy of one. This leads to the large difference between our model and mixture models in the description of water anomaly.<sup>42,71</sup>

**Physical Explanation of the Glass-Forming Ability and Fragility in a Water/LiCl Mixture.** Now we discuss the experimental results of water/LiCl mixtures in light of the above two-order-parameter model. The tetrahedral structure of water molecules can be regarded as LFS also in the case of the water/LiCl mixture. As we mentioned in the Introduction, adding salt has a similar effect to applying pressure to destroy the tetrahedral order in water. Addition of LiCl to water leads to the formation of a hydration shell around a small  $\text{Li}^+$  ion and the resulting destabilization of LFS:<sup>1</sup> LiCl acts as a hydrogen bond (more specifically, LFS) breaker. This picture is supported by recent numerical simulations: reduction of tetrahedral structures with an increase in the salt concentration has been concluded from a change in the OO-pair correlation function by molecular dynamics simulations.<sup>84</sup> Strictly speaking, we can consider more than two types of LFSS, a tetrahedral structure stabilized by hydrogen bonding and a hydration structure stabilized by monopole (ion;  $\text{Li}^+$  and  $\text{Cl}^-$ )–dipole (water) interactions. However, since the number density of the former should be anticorrelated with that of the latter, it may be enough to consider only the tetrahedral one as LFS for our qualitative argument for a while.

We observed how the tetrahedral structure of water molecules reduces with increasing LiCl concentration  $\phi$  by Raman scattering measurements. Here we extend the expression of the pressure  $P$  dependence of number density of LFS in eq 5 to the salt concentration  $\phi$ . In addition to the energy difference  $\Delta E$  between NLS and LFS, we introduce the chemical potential difference linked to the salt concentration as  $\Delta\mu$ . The latter expresses the fact that addition of salt by  $\phi$  destabilizes LFS by  $\Delta\mu\phi$ . Then, the average fraction of LFS,  $S$ , is given by the following Boltzmann factor

$$S(\phi) = S_0 \exp[(\Delta E - \phi\Delta\mu)/k_B T] \quad (6)$$

For pure water ( $\phi = 0$ ), we estimated  $\Delta E/k_B = 1800$  K and  $S_0 = 8.1 \times 10^{-5}$ .<sup>42,71</sup>

The parameter  $C$  obtained by Raman scattering measurements may not be directly equal to  $S$ , but we expect that  $C$  is proportional to it at least in the first approximation. This relation between  $C$  and  $S$  may be similar to the relation between the tetrahedral order parameter  $q$  deduced from real dynamics and from inherent dynamics.<sup>64,65</sup> We fitted  $C(\phi) = kS(\phi)$  to the data by using  $k$  and  $\Delta\mu$  as the adjustable parameters. The fitting result with  $\Delta\mu/k_B = 2590$  K is shown in Figure 17. The agreement is reasonably good. The results suggest that the number density of locally favored tetrahedral order decreases with an increase in  $\phi$ , obeying at least approximately the Boltzmann factor  $S(\phi)$  (see above): LiCl acts as breakers of local tetrahedral order.

We checked the volume change  $\Delta V_{\text{cry}}$  due to crystallization to identify the type of crystal ( $\rho$  or  $S$ ). Pure water is known to exhibit a large volume increase upon crystallization. Although the

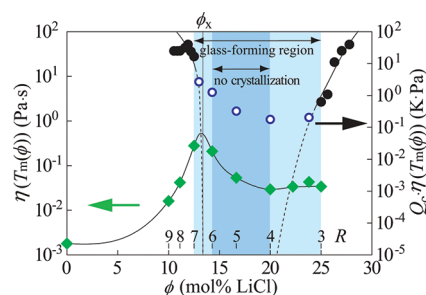


**Figure 18.**  $\phi$ -dependences of  $\eta$  at  $T_m(\phi)$ ,  $\eta(T_m(\phi))$ , and  $Q_c \cdot \eta$ .  $\eta$  reaches its maximum value around  $R = 6.5$  where the stable crystal structure changes from ice  $I_h$  to hydrates. The high glass-forming ability around  $R = 4$ – $5$  cannot be explained by the increase of  $\eta$  around  $\phi_x$  alone.

volume change is not as distinct as for pure water, Fornazero et al. reported the volume increase in  $R = 8.56$  from density measurements.<sup>85</sup> For a sample of  $R = 3$ , on the other hand, we confirmed by eye inspection a distinct volume decrease upon crystallization as in ordinary liquids. These facts imply that  $\Delta V_{\text{cry}}$  changes its sign from positive to negative by adding LiCl, supporting the existence of a change in the stable crystal structure from  $S$ -crystal to  $\rho$ -crystal (see Figure 2).

The glass-forming ability (GFA) of water/LiCl mixtures is explained as follows. At a low LiCl concentration  $\phi$  (i.e., at large  $R$ ), the situation is similar to that of pure water. Ice  $I_h$  is easily formed due to its consistency with the tetrahedral structure of LFS: very poor glass-forming ability. With an increase in the LiCl concentration, the decrease in tetrahedral LFSS and the increase in hydrated structures make water more difficult to form the hexagonal ice crystal. For LiCl concentrations where the melting curve for  $S$ -crystal (ice  $I_h$ ) is still higher than the extrapolated melting curve for  $\rho$ -crystal (hydrate crystals), ice  $I_h$  may be more easily formed than a hydrate crystal upon cooling. At temperatures below the two melting curves, there is a competition between the two types of crystal orderings, suggesting a less chance of crystallization.<sup>31,32</sup> Thus, the temperature region between the melting curve for ice  $I_h$  and the extrapolated curve for a hydrate crystal is a dangerous zone for crystallization. When approaching the composition  $\phi_x$  at which  $T_m$  has the minimum, with an increase in the LiCl concentration the duration time passing through this dangerous zone upon cooling becomes shorter, which should increase the glass-forming ability. For a LiCl concentration above  $\phi_x$ , LFS finally becomes incompatible with the equilibrium crystal structure, which is “ $\text{LiCl} \cdot \text{RH}_2\text{O}$  crystal”. This situation for  $\phi > \phi_x$  is similar to ordinary liquids, for which  $\Delta V_{\text{cry}} < 0$ . In this region, an increase in  $\phi$  leads to further breaking of tetrahedral LFSS, which decreases the degree of frustration. This should result in the decrease in the glass-forming ability and the increase in the fragility. This is similar to the pressure-induced increase in the fragility observed in our numerical simulations of spin liquids.<sup>86</sup>

We consider also the kinetic contribution to the GFA. A similar V-shaped phase diagram and high GFA around the eutectic point are features common to metallic systems.<sup>31,87</sup> It is generally explained by the fact that the viscosity of an equilibrium liquid just above the melting point is higher simply because the melting point is minimum at the eutectic point. For our water/LiCl system, we plotted the  $\phi$ -dependence of  $\eta$  at  $T_m(\phi)$  in Figure 18. Reflecting the lower  $T_m$  near the triple point,

$\eta$  has a maximum near  $\phi_x$  ( $R_x \sim 6.5$ ). However, this kinetic factor alone cannot explain the steep minimum of the critical cooling rate  $Q_c$  around  $R = 4-5$  (see Figure 4). Viscosity shows a similar value at both  $R = 8$  and  $R = 5$ , but the GFA is quite different. A sample of  $R = 8$  is so easy to crystallize, whereas we have never seen any crystallization for  $R = 5$ . This is evident from the very deep minimum in  $Q_c \cdot \eta$  near  $\phi_x$  shown in Figure 18. These results indicate the importance of a thermodynamic factor, i.e., the energetic frustration, besides the kinetic factor.

We expect that fragility has a negative correlation with GFA; however, the fragility shows a monotonic increase with an increase in the LiCl concentration  $\phi$  in the region we investigated, unlike GFA. We should consider frustration effects of the tetrahedral structure of LFS against the “LiCl·RH<sub>2</sub>O crystal” structure of the corresponding concentration, not against the ice I<sub>h</sub> structure. The formation of ice I<sub>h</sub> at low LiCl concentrations is just a manifestation of the existence of a stable S-crystal and the consistency of LFS and the S-crystal. Thus, the addition of LiCl should make water more fragile monotonically. The behavior of the fragility index  $D$  and  $m$  is also consistent with our other findings, e.g., the  $R$ -dependence of  $T_0$  (see Table 1 and Figure 2), on noting that a more fragile liquid should have a smaller distance between  $T_m$  (the onset of cooperativity) and  $T_0$  (the divergence temperature).

**Quantitative Description of the Dependence of Viscosity on the LiCl Concentration.** We showed the  $\phi$ -dependence of  $\eta$  for several temperatures in Figure 7. At low temperatures,  $\eta$  first decreases upon the addition of LiCl, but its further addition leads to the increase in  $\eta$  due to the structuring of water around Li<sup>+</sup> ions (hydration). This nonmonotonic behavior is strikingly similar to the pressure dependence of the viscosity, which further supports the equivalence of pressure and salt effects on the behavior of water. To make this link more quantitative, we consider the  $\phi$ -dependence of the viscosity  $\eta$  on the basis of our two-order-parameter model.

We explained the viscosity anomaly of water as a function of pressure as follows.<sup>32,42,71</sup> In usual liquids, the activation energy required for viscous flow or diffusion is associated with the creation of a hole or the disruption of local interactions with its neighboring molecules. We express this normal contribution to the activation energy as  $E_a^{BP} = E_B + \Delta\nu_a P$ , where  $\Delta\nu_a$  is the volume difference between the activated state and the initial normal state. The existence of the unique activation energy for this process is the origin of the Arrhenius behavior. Under the existence of LFS, however, an additional activation energy,  $\Delta E_a^P$ , is required for molecules participating in these structures to flow. Here we note that the lifetime of LFS, which is longer than that of NLS, is still quite short ( $\ll$  microsecond), and thus a liquid cannot be regarded as a mixture of stable NLS and LFS. Thus, the activation energy averaged over all molecules participating and not participating LFS is estimated as

$$E_a^P(T, P) = E_a^{BP}(P) + \Delta E_a^P S(T, P) \quad (7)$$

where  $E_a^{BP}$  is the background activation energy for normal water without LFSs.

Here we extend this argument to the case of the  $\phi$ -dependence of  $\eta$ . In the case of a water/LiCl mixture, there are two types of low-energy structures. One is LFS stabilized by hydrogen bonding, and the other is a hydration structure around an ion. The former decreases with an increase in  $\phi$ , as expressed by eq 6, whereas the latter should increase. The fraction of ions having

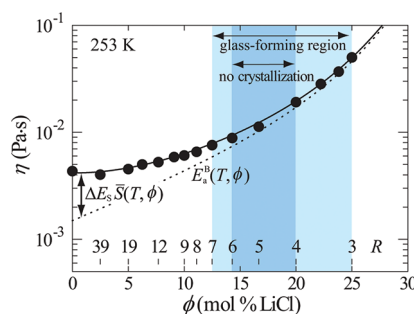


**Figure 19.**  $\phi$ -dependence of the viscosity  $\eta$  at 253 K. The solid curve is the result of our fitting, whereas the dotted curve is the background contribution  $E_a^B(T, \phi)$  besides the contribution of locally favored tetrahedral structures.

hydration structures,  $M$ , may be expressed as

$$M \cong M_0 \exp((\Delta E_{\text{ion}} + \Delta\mu_{\text{ion}}\phi)/k_B T) \quad (8)$$

where  $\Delta E_{\text{ion}}$  and  $\Delta\mu_{\text{ion}}$  is the difference in the energy and chemical potential between hydrated and nonhydrated water structures, respectively. Then the activation energy for shear flow may be expressed by the sum of the activation energy for normal liquid structures of water  $E_B$ , the mixing contribution  $\Delta E_N\phi$ , the contribution of hydrated structures  $\Delta E_M\phi M$ , and that of locally favored tetrahedral structures  $\Delta E_S S$ . We express the sum of the first three contributions as the background part  $E_a^B$ . In this way, the total activation energy for viscous transport,  $E_a$ , is given by

$$E_a(T, \phi) = E_a^B(T, \phi) + \Delta E_S S(T, \phi) \quad (9)$$

$$E_a^B(T, \phi) = E_B + \Delta E_N\phi + \Delta E_M\phi M(T, \phi) \quad (10)$$

The  $T, \phi$ -dependence of the viscosity is thus predicted as

$$\eta(T, \phi) \cong \eta_0 T^{3/2} \exp[E_a(T, \phi)/k_B T] \quad (11)$$

The fitting of eq 11 to the  $\phi$ -dependence of viscosity for several temperatures is shown in Figure 7(b). In the fitting, we used the common parameters for the data at all different temperatures. The agreement is satisfactory, on noting this. We used  $E_B/k_B = 1832$  K,  $\Delta E_S/k_B = 2612$  K,  $\Delta E/k_B = 1800$  K, and  $\eta_0 = 2.66 \times 10^{-10}$  Pa·s, which were independently determined for pure water.<sup>32,42</sup> The value of  $\Delta\mu/k_B = 2590$  K was also independently determined from the fitting to  $C(\phi)$  (see above and Figure 17). From the fitting of eq 11 to the data of  $\eta(T, \phi)$ , we obtain  $\Delta E_N/k_B = 2478$  K,  $\Delta E_{\text{ion}}/k_B = 660$  K,  $\Delta\mu_{\text{ion}}/k_B = 2440$  K, and  $\Delta E_M \cdot M_0/k_B = 0.065$  K.

In Figure 19, we show the result of our fitting for  $T = 253$  K. The solid curve is our fit to eq 11, which nicely reproduces the  $\phi$ -dependence of  $\eta$ , and the dashed curve is the background part,  $E_a^B(T, \phi)$ . The results shown in Figure 19 and Figure 7 tell us that the nonmonotonic  $\phi$ -dependence of the viscosity at low temperatures is a consequence of the reduction of the number density of locally favored tetrahedral structures (proportional to  $S(T, \phi)$ ) with an increase in  $\phi$ . This is clear evidence for the fact that addition of salt to water induces breakage of tetrahedral order. Thus, we can say that in addition to the thermodynamic and structural evidence for salt-induced breakage of tetrahedral order<sup>26,27</sup> our results provide strong “dynamic” evidence for it.

**Pressure Dependence of the Glass-Forming Ability and Fragility of Pure Water.** Easier vitrification of water under high pressure was known for a long time. For example, Sartori et al.<sup>88</sup>



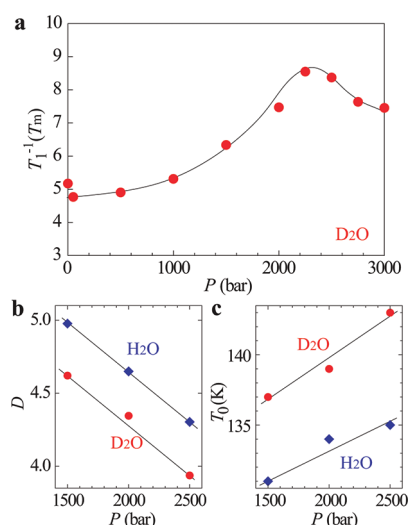


**Figure 20.** Pressure dependence of kinetic properties of pure water estimated from NMR relaxation.<sup>92</sup> (a) The  $P$ -dependence of the characteristic relaxation time  $X = T_1^{-1}$  for deuterated water  $D_2O$  at the melting point  $T_m(P)$ .  $T_1^{-1}$  has a maximum around the triple point. The solid curve is a guide to the eyes. (b) The fragility index  $D$  and (c) the ideal glass transition temperature  $T_0$  obtained by VFT fits to  $X(T) = T_1^{-1}(T)$  for  $H_2O$  and  $D_2O$ . The fragility increases with an increase in pressure. Solid lines are guides to the eyes.

showed that for a given cooling rate the thickness of an aqueous sample that can be vitrified can be increased ten times by high-pressure quenching. Recently, Mishima and Suzuki<sup>19</sup> performed more quantitative measurements for emulsified water. They vitrified water by rapidly cooling emulsified water under a high pressure around 2–3 kbar, and the critical quenching rate required for vitrification is about  $10^3$  K/s. This cooling rate is much slower than the cooling rate required for vitrifying emulsified water at ambient pressure, about  $\sim 10^6$  K/s.<sup>19,89</sup> The cooling rate required for vitrification seems to become faster in an even higher pressure region of 5–7 kbar.<sup>90</sup> On this issue of pressure effects on vitrification of water, please also refer to a review by Angell.<sup>91</sup>

The glass-forming ability can be affected by the kinetic factor determined by the transport in a liquid; however, it is not enough to explain the above drastic change in the critical cooling rate, as emphasized above. We estimated the relaxation time of deuterated water from the nuclear magnetic resonance (NMR) data reported by Lang and Lüdemann<sup>92</sup> at  $T_m(P)$  as a function of  $P$ . The results are shown in Figure 20(a), which indicates that the characteristic relaxation time  $X \cong T_1^{-1}$  is longer near the triple point. Note that  $X$  is inversely proportional to the deuteron spin–lattice relaxation time  $T_1$  when  $\omega_0\tau \ll 1$ , where  $\omega_0$  is the NMR resonant frequency and  $\tau$  is the relaxation time. This is very similar to the peaking of the viscosity at  $T_m(\phi)$  around the triple point for water/LiCl mixtures (see Figure 18), although the magnitude of the change as a function of pressure is very weak (less than a factor of 2). This weak peaking does not explain the change of the critical cooling rate in 3 orders of magnitude mentioned above.

On the pressure dependence of the glass-forming ability, the distance between the melting point  $T_m$  and the homogeneous nucleation temperature  $T_H$  may also be a useful measure characterizing it. In Figure 21, we show a  $T$ – $P$  phase diagram of pure water as well as the pressure dependence of  $(T_m - T_H)/T_m$

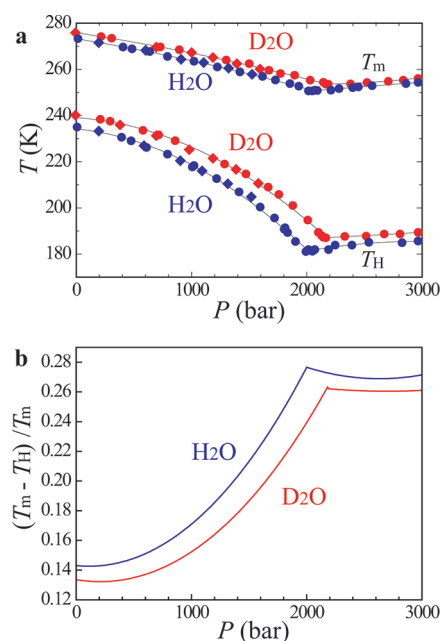


**Figure 21.** (a) Phase diagram of pure water. These data were reported for  $H_2O$  or  $D_2O$  emulsions in methylcyclohexane + methylcyclopentane (circles) and in  $n$ -heptane (diamonds).<sup>93,94</sup> (b)  $P$ -dependence of the distance between the melting and homogeneous nucleation temperature normalized by  $T_m$ ,  $(T_m - T_H)/T_m$ , for  $H_2O$  and  $D_2O$ . The distance increases with an increase in pressure. There is a change in the trend at the triple point. Both curves were calculated from the phase diagram (a).

which was estimated from the data of  $T_m$  and  $T_H$ .<sup>93,94</sup> With an increase in pressure  $P$ , the value of  $(T_m - T_H)/T_m$  monotonically increases until reaching  $P_x \sim 2$  kbar, and then it almost becomes independent with pressure (but the data are limited below 3 kbar), suggesting the increase in the glass-forming ability with a pressure increase toward the triple point. We may at least say that the glass-forming ability of water is higher for above  $P_x$  than for below  $P_x$ . This quantity,  $T_m - T_H$ , which is a measure of the maximum degree of supercooling, mainly reflects the thermodynamic barrier for crystal nucleation.

The pressure dependence of the fragility of pure water was studied by Lang and Lüdemann by NMR measurements.<sup>92</sup> They measured the deuteron spin–lattice relaxation time  $T_1$  and analyzed the results by using the Vogel–Fulcher–Tamman relation  $X = X_0 \exp(DT_0/(T - T_0))$ , where  $X$  is the characteristic time of structural relaxation (see above). They obtained the values of the fragility index  $D$  and the ideal glass-transition temperature  $T_0$  by the VFT fitting, and the result is plotted in Figure 20(b) and (c).<sup>92</sup> The decrease of  $D$  and the increase of  $T_0$  with an increase in pressure both indicate that liquid water becomes more fragile with an increase in pressure in the above pressure range. This is consistent with our prediction that the fragility should increase with increasing pressure near and above the triple point, as well as our results for water/LiCl mixtures.

**Relation to Other Systems.** The above physical picture tells us that the same scenario should hold for any system having the V-shaped phase diagram. The V-shaped phase diagram is a common property of water-type liquids such as Si, Ge, and eutectic mixtures.<sup>31</sup> Our scenario predicts a high glass-forming ability around the minimum of a melting curve, a triple point.<sup>31,32</sup> Such a link of the strength of frustration to the fragility and the glass-forming ability has been confirmed by both simulations and

experiments. Here we mention some of these examples. Our simulations showed that vitrification can be achieved by increasing the strength of frustration, and the fragility increases with an increase in frustration in two-dimensional (2D) spin liquids<sup>67,86</sup> and 2D and 3D polydisperse colloidal liquids.<sup>69,68,70</sup> Angell and his co-workers also succeeded in vitrifying a monatomic Si-like liquid with the Stillinger–Weber potential in their molecular dynamics simulations by controlling the strength of frustration and showed the high GFA of liquid around the triple point.<sup>95</sup> Along the same spirit, furthermore, they succeeded in experimentally forming a monatomic “metallic” glass of Ge at a pressure near the triple point.<sup>96</sup>

Applying pressure induces the increase or decrease of the number density of LFS for  $\Delta V < 0$  or  $\Delta V > 0$ , respectively. Instead of changing pressure, we can add additives to a liquid to modify the number density of LFS, which allows us to control the glass-forming ability and the fragility of a liquid in a systematic way. Typical examples are salt for water<sup>22,24,25</sup> and  $\text{Na}_2\text{O}$  for  $\text{SiO}_2$ .<sup>21</sup> The similar behavior has also been reported for  $\text{Ca}(\text{NO}_3)_2$ – $\text{KNO}_3$  systems.<sup>97</sup> The same scenario may also be applied to various materials having a V-shaped phase diagram, e.g., metallic systems having a deep eutectic. It has been known empirically that the glass-forming ability of a multicomponent metallic glass former increases while approaching a deep eutectic point. This was explained by the fact that the viscosity of an equilibrium liquid just above the melting point is higher simply because the melting point is minimum at the eutectic point. Our study shows that this kinetic argument may not be enough. We propose that there is another important factor: near a eutectic point two types of local structures linked to crystals compete, leading to stronger energetic frustration against crystallization, which helps glass formation.<sup>98</sup> Such behavior was indeed observed by simulations.<sup>99,100</sup> In other words, the thermodynamic factor, more specifically, energetic and geometrical frustration, may also play a crucial role in the high glass-forming ability in addition to the kinetic factor, in general.

## V. SUMMARY

In summary, we experimentally demonstrated an intimate link of the shape of the “equilibrium” phase diagram (Figure 1 and Figure 2) to the “nonequilibrium” glass transition behavior including the liquid fragility (Figure 10 and Figure 14) and the glass-forming ability (Figure 4). This suggests a remarkable possibility of predicting the glass-forming ability and the fragility of a liquid from the shape of its equilibrium phase diagram. The key is the relationship between global minimization of the free energy toward crystal and local minimization toward LFS. Depending upon the consistency of these two symmetries, LFS can be either a promoter of crystallization or its preventer. This physical picture tells us that a physical factor making water so unusual among molecular liquids is the V-shaped  $P$ – $T$  phase diagram, which is a consequence of the transition from an  $S$ -crystal to a  $\rho$ -crystal with increasing  $P$  (see Figure 1): water may be the only molecular liquid having such a phase diagram. We argue that a V-shaped phase diagram is in general a manifestation of underlying competing orderings, as described above. This may also be the case for strongly correlated electronic systems (see, e.g., Figure 2 of ref 101). Our finding may shed new light on a general mechanism of glass transition itself. It may also provide a simple physical principle for enhancing the glass-forming ability of liquid.

In this paper, we did not touch the possibility of a hidden liquid–liquid transition in water and water-type liquids.<sup>3,102</sup> This is linked to the cooperativity in the formation of locally favored structures. It is natural to expect such cooperativity in tetrahedral ordering, and thus, this is an interesting topic for future research. It is worth mentioning that experimental studies toward this direction were performed by Mishima and Suzuki for water/ $\text{LiCl}$  mixtures.<sup>34,35</sup>

## AUTHOR INFORMATION

### Corresponding Author

\*E-mail: tanaka@iis.u-tokyo.ac.jp.

## ACKNOWLEDGMENT

We are very happy to dedicate this contribution to Prof. Gene Stanley, who pioneered the statistical physics of water. The authors thank C. Austen Angell for valuable discussion and encouragement and also for kindly notifying us of a few important references. They are grateful to George Floudas for stimulating discussions on the determination of fragility by calorimetry and the crystal structure trace from diffraction data. Yoshiharu Suzuki is greatly acknowledged for the information on the emulsified water under pressure. We also thank Anke Kaltbeitzel, Petra Räder, and Doris Vollmer for technical support for DSC measurements. This work was partially supported by a grant-in-aid from the Ministry of Education, Culture, Sports, Science and Technology, Japan.

## REFERENCES

- (1) Eisenberg, D.; Kauzmann, W. *The Structure and Properties of Water*; Oxford University Press: New York, 1969.
- (2) Angell, C. A. *Science* **1995**, *267*, 1924–1935.
- (3) Mishima, O.; Stanley, H. E. *Nature* **1998**, *396*, 329–335.
- (4) Debenedetti, P. G. *J. Phys.: Condens. Matter* **2003**, *15*, R1669–R1726.
- (5) Angell, C. A. *Science* **2008**, *319*, 582–587.
- (6) Soper, A. K. *Mol. Phys.* **2008**, *106*, 2053–2076.
- (7) Wowk, B.; Darwin, M.; Harris, S. B.; Russell, S. R.; Rasch, C. M. *Cryobiology* **1999**, *39*, 215–227.
- (8) Matsumoto, M.; Saito, S.; Ohmine, I. *Nature* **2002**, *416*, 409–413.
- (9) Sastry, S. *Nature* **2002**, *416*, 376–377.
- (10) Yamada, M.; Mossa, S.; Stanley, H. E.; Sciortino, F. *Phys. Rev. Lett.* **2002**, *88*, 195701.
- (11) Radhakrishnan, R.; Trout, B. L. *Phys. Rev. Lett.* **2003**, *90*, 158301.
- (12) Loerting, T.; Giovambattista, N. *J. Phys.: Condens. Matter* **2006**, *18*, R919–R977.
- (13) Giovambattista, N.; Angell, C. A.; Sciortino, F.; Stanley, H. E. *Phys. Rev. Lett.* **2004**, *93*, 047801.
- (14) Velikov, V.; Borick, S.; Angell, C. A. *Science* **2001**, *294*, 2335–2338.
- (15) Johari, G. P. *J. Chem. Phys.* **2002**, *116*, 8067–8073.
- (16) Finney, J. L.; Hallbrucker, A.; Kohl, I.; Soper, A. K.; Bowron, D. T. *Phys. Rev. Lett.* **2002**, *88*, 225503.
- (17) Johari, G. P.; Hallbrucker, A.; Mayer, E. J. *J. Chem. Phys.* **1991**, *95*, 6849–6855.
- (18) Gromnitskaya, E. L.; Stal'gorova, O. V.; Brazhkin, V. V.; Lyapin, A. G. *Phys. Rev. B* **2001**, *64*, 094205.
- (19) Mishima, O.; Suzuki, Y. *J. Chem. Phys.* **2001**, *115*, 4199–4202.
- (20) Kanno, H.; Angell, C. A. *J. Phys. Chem.* **1977**, *81*, 2639–2643.
- (21) Angell, C. A.; Sare, E. J. *J. Chem. Phys.* **1968**, *49*, 4713–4714.
- (22) Angell, C. A.; Sare, E. J. *J. Chem. Phys.* **1970**, *52*, 1058–1068.

- (23) Angell, C. A.; Bressel, R. D.; Green, J. L.; Kanno, H.; Oguni, M.; Sare, E. J. *J. Food Eng.* **1994**, *22*, 115–142.
- (24) Angell, C. A. *Chem. Rev.* **2002**, *102*, 2627–2650.
- (25) Prével, B.; Jal, J. F.; Dupuy-Philon, J.; Soper, A. K. *J. Chem. Phys.* **1995**, *103*, 1886–1896.
- (26) Leberman, R.; Soper, A. K. *Nature* **1995**, *378*, 364–366.
- (27) Green, J. L.; Lacey, A. R.; Sceats, M. G. *Chem. Phys. Lett.* **1987**, *134*, 385–391.
- (28) Stillinger, F. H.; Ben-Naim, A. *J. Phys. Chem.* **1969**, *73*, 900–907.
- (29) Mudi, A.; Chakravarty, C. *J. Phys. Chem. B* **2006**, *110*, 8422–8431.
- (30) Smith, J. D.; Saykally, R. J.; Geissler, P. L. *J. Am. Chem. Soc.* **2007**, *129*, 13847–13856.
- (31) Tanaka, H. *Phys. Rev. B* **2002**, *66*, 064202.
- (32) Tanaka, H. *J. Phys.: Condens. Matter* **2003**, *15*, L703–L711.
- (33) Kobayashi, M.; Tanaka, H. *Phys. Rev. Lett.* **2011**, *106*, 125703.
- (34) Suzuki, Y.; Mishima, O. *Phys. Rev. Lett.* **2000**, *85*, 1322–1325.
- (35) Suzuki, Y.; Mishima, O. *J. Chem. Phys.* **2002**, *117*, 1673–1676.
- (36) Tanaka, H. *J. Phys.: Condens. Matter* **1998**, *10*, L207–L214.
- (37) Tanaka, H. *J. Chem. Phys.* **1999**, *111*, 3163–3174.
- (38) Tanaka, H. *J. Chem. Phys.* **1999**, *111*, 3175–3182.
- (39) Tanaka, H. *J. Non-Cryst. Solids* **2005**, *351*, 3371–3384.
- (40) Elarby-Aouizerat, A.; Jal, J.-F.; Chieux, P.; Letoffé, J. M.; Claudy, P.; Dupuy, J. *J. Non-Cryst. Solids* **1988**, *104*, 203–210.
- (41) Bett, K. E.; Cappi, J. B. *Nature* **1965**, *207*, 620–621.
- (42) Tanaka, H. *J. Chem. Phys.* **2000**, *112*, 799–809.
- (43) Wang, L.-M.; Angell, C. A. *J. Chem. Phys.* **2003**, *118*, 10353–10355.
- (44) Plazek, D. J.; Ngai, K. L. *Macromolecules* **1991**, *24*, 1222–1224.
- (45) Böhmer, R.; Angell, C. A. *Phys. Rev. B* **1992**, *45*, 10091–10094.
- (46) Moynihan, C. T.; Easteal, A. J.; Wilder, J.; Tucker, J. *J. Phys. Chem.* **1974**, *78*, 2673–2677.
- (47) Moura Ramos, J. J.; Taveira-Marques, R.; Diogo, H. P. *J. Pharm. Sci.* **2004**, *93*, 1503–1507.
- (48) Moynihan, C. T.; Lee, S.-K.; Tatsumisago, M.; Minami, T. *Thermochim. Acta* **1996**, *280/281*, 153–162.
- (49) Wang, L.-M.; Angell, C. A.; Richert, R. *J. Chem. Phys.* **2006**, *125*, 074505.
- (50) Diogo, H. P.; Pinto, S. S.; Moura Ramos, J. J. *Carbohydr. Res.* **2007**, *342*, 961–969.
- (51) Böhmer, R.; Ngai, K. L.; Angell, C. A.; Plazek, D. J. *J. Chem. Phys.* **1993**, *99*, 4201–4209.
- (52) Richardson, M. J.; Savill, N. G. *Polymer* **1975**, *16*, 753–757.
- (53) Simatos, D.; Blond, G.; Roudaut, G.; Champion, D.; Perez, J.; Favre, A. L. *J. Therm. Anal.* **1996**, *47*, 1419–1436.
- (54) Walrafen, G. E. *J. Chem. Phys.* **1967**, *47*, 114–126.
- (55) Walrafen, G. E. *J. Chem. Phys.* **1962**, *36*, 1035–1042.
- (56) Green, J. L.; Lacey, A. R.; Sceats, M. G. *J. Phys. Chem.* **1986**, *90*, 3958–3964.
- (57) Paolantoni, M.; Faginas Lago, N.; Alberti, M.; Laganà, A. *J. Phys. Chem. A* **2009**, *113*, 15100–15105.
- (58) Falk, M.; Ford, T. A. *Can. J. Chem.* **1966**, *44*, 1699–1707.
- (59) Smith, J. D.; Cappa, C. D.; Wilson, K. R.; Cohen, R. C.; Geissler, P. L.; Saykally, R. J. *Proc. Natl. Acad. Sci. U.S.A.* **2005**, *102*, 14171–14174.
- (60) Auer, B. M.; Skinner, J. L. *J. Chem. Phys.* **2008**, *128*, 224511.
- (61) Fecko, C. J.; Eaves, J. D.; Loparo, J. J.; Tokmakoff, A.; Geissler, P. L. *Science* **2003**, *301*, 1698–1702.
- (62) Auer, B.; Kumar, R.; Schmidt, J. R.; Skinner, J. L. *Proc. Natl. Acad. Sci. U.S.A.* **2007**, *104*, 14215–14220.
- (63) Lin, Y.-S.; Auer, B. M.; Skinner, J. L. *J. Chem. Phys.* **2009**, *131*, 144511.
- (64) Appignanesi, G. A.; Rodriguez Fris, J. A.; Sciortino, F. *Eur. Phys. J. E* **2009**, *29*, 305–310.
- (65) Accordino, S. R.; Rodriguez Fris, J. A.; Sciortino, F.; Appignanesi, G. A. *Eur. Phys. J. E* **2011**, *34*, 48.
- (66) Tanaka, H. *J. Stat. Mech.* **2010**, P12001.
- (67) Shintani, H.; Tanaka, H. *Nat. Phys.* **2006**, *2*, 200–206.
- (68) Tanaka, H.; Kawasaki, T.; Shintani, H.; Watanabe, K. *Nat. Mater.* **2010**, *9*, 324–331.
- (69) Kawasaki, T.; Araki, T.; Tanaka, H. *Phys. Rev. Lett.* **2007**, *99*, 215701.
- (70) Kawasaki, T.; Tanaka, H. *J. Phys.: Condens. Matter* **2010**, *22*, 232102.
- (71) Tanaka, H. *Europhys. Lett.* **2000**, *50*, 340–346.
- (72) Huang, C.; et al. *Proc. Natl. Acad. Sci. U.S.A.* **2009**, *106*, 15214–15218.
- (73) Tanaka, H. *Phys. Rev. E* **2000**, *62*, 6968–6976.
- (74) Kumar, P.; Buldyrev, S. V.; Stanley, H. E. *Proc. Natl. Acad. Sci. U.S.A.* **2009**, *106*, 22130–22134.
- (75) Agarwal, M.; Alam, M. P.; Chakravarty, C. *J. Phys. Chem. B* **2011**, *115*, 6935–6945.
- (76) Tanaka, H. *Phys. Rev. Lett.* **1998**, *80*, 5750–5753.
- (77) Errington, J. R.; Debenedetti, P. G. *Nature* **2001**, *409*, 318–321.
- (78) Sharma, R.; Chakraborty, S. N.; Chakravarty, C. *J. Chem. Phys.* **2006**, *125*, 204501.
- (79) Mittal, J.; Errington, J. R.; Truskett, T. M. *J. Phys. Chem. B* **2006**, *110*, 18147–18150.
- (80) Mittal, J.; Errington, J. R.; Truskett, T. M. *J. Chem. Phys.* **2006**, *125*, 076102.
- (81) Agarwal, M.; Singh, M.; Sharma, R.; Alam, M. P.; Chakravarty, C. *J. Phys. Chem. B* **2010**, *114*, 6995–7001.
- (82) de Oliveira, A. B.; Salcedo, E.; Chakravarty, C.; Barbosa, M. C. *J. Chem. Phys.* **2010**, *132*, 234509.
- (83) Kamb, B. *Science* **1965**, *150*, 205–209.
- (84) Mountain, R. D. *Int. J. Thermophys.* **2007**, *28*, 536–543.
- (85) Fornazero, J.; El Hachadi, A.; Dupuy-Philon, J. *J. Non-Cryst. Solids* **1992**, *150*, 413–418.
- (86) Shintani, H.; Tanaka, H. *Nat. Mater.* **2008**, *7*, 870–877.
- (87) Tanaka, H. *J. Non-Cryst. Solids* **2005**, *351*, 678–690.
- (88) Sartori, N.; Richter, K.; Dubochet, J. *J. Microsc.* **1993**, *172*, 55–61.
- (89) Brüggeller, P.; Mayer, E. *Nature* **1980**, *288*, 569–571.
- (90) Suzuki, Y. private communication. We thank Dr. Y. Suzuki for providing us with valuable information on the GFA of emulsified water at high pressures.
- (91) Angell, C. A. *Annu. Rev. Phys. Chem.* **2004**, *55*, 559–583.
- (92) Lang, E. W.; Lüdemann, H.-D. *Angew. Chem., Int. Ed. Engl.* **1982**, *21*, 315–329.
- (93) Kanno, H.; Speedy, R. J.; Angell, C. A. *Science* **1975**, *189*, 880–881.
- (94) Angell, C. A.; Kanno, H. *Science* **1976**, *193*, 1121–1122.
- (95) Molinero, V.; Sastry, S.; Angell, C. A. *Phys. Rev. Lett.* **2006**, *97*, 075701.
- (96) Bhat, M. H.; Molinero, V.; Soignard, E.; Solomon, V. C.; Sastry, S.; Yarger, J. L.; Angell, C. A. *Nature* **2007**, *448*, 787–791.
- (97) Senapati, H.; Kadiyala, R. K.; Angell, C. A. *J. Phys. Chem.* **1991**, *95*, 7050–7054.
- (98) Tanaka, H. *J. Phys.: Condens. Matter* **2003**, *15*, L491–L498.
- (99) Jakse, N.; Pasturel, A. *Phys. Rev. B* **2008**, *78*, 214204.
- (100) Pasturel, A.; Tasci, E. S.; Sluiter, M. H. F.; Jakse, N. *Phys. Rev. B* **2010**, *81*, 140202(R).
- (101) Dagotto, E. *Science* **2005**, *309*, 257–262.
- (102) Poole, P. H.; Sciortino, F.; Essmann, U.; Stanley, H. E. *Nature* **1992**, *360*, 324–328.
- (103) Hallett, J. *Proc. Phys. Soc.* **1963**, *82*, 1046–1050.
- (104) Korson, L.; Drost-Hansen, W.; Millero, F. J. *J. Phys. Chem.* **1969**, *73*, 34–39.
- (105) Osipov, Y. A.; Zheleznyi, B. V.; Bondarenko, N. F. *Russ. J. Phys. Chem.* **1977**, *51*, 748–749.